BIOCHEMISTRY

© Copyright 2005 by the American Chemical Society Volume 44, Number 6 February 15, 2005

Articles

Crystal Structure and Solution NMR Dynamics of a D (Type II) Peroxiredoxin Glutaredoxin and Thioredoxin Dependent: A New Insight into the Peroxiredoxin Oligomerism†

Aude Echalier,‡,§ Xavier Trivelli,§,|| Catherine Corbier,‡ Nicolas Rouhier,⊥ Olivier Walker,|| Pascale Tsan,|| Jean-Pierre Jacquot,⊥ André Aubry,‡ Isabelle Krimm,*,|| and Jean-Marc Lancelin*,||

LCM3B, Groupe Biocristallographie, Université Henri Poincaré—Nancy1, UMR CNRS 7036, 54506 Vandoeuvre, France, RMN Biomoléculaire, Université Claude Bernard—Lyon1, UMR CNRS 5180 Sciences Analytiques, ESCPE-Lyon, 69622 Villeurbanne, France, and UMR Interaction Arbres Microorganismes, Université Henri Poincaré—Nancy1, UMR INRA 1136, 54506 Vandoeuvre, France

Received August 17, 2004; Revised Manuscript Received October 22, 2004

ABSTRACT: Peroxiredoxins (Prxs) constitute a family of thiol peroxidases that reduce hydrogen peroxide, peroxinitrite, and hydroperoxides using a strictly conserved cysteine. Very abundant in all organisms, Prxs are produced as diverse isoforms characterized by different catalytic mechanisms and various thiol-containing reducing agents. The oligomeric state of Prxs and the link with their functionality is a subject of intensive research. We present here a combined X-ray and nuclear magnetic resonance (NMR) study of a plant Prx that belongs to the D-Prx (type II) subfamily. The *Populus trichocarpa* Prx is the first Prx shown to be regenerated *in vitro* by both the glutaredoxin and thioredoxin systems. The crystal structure and solution NMR provide evidence that the reduced protein is a specific noncovalent homodimer both in the crystal and in solution. The dimer interface is roughly perpendicular to the plane of the central β sheet and differs from the interface of A- and B-Prx dimers, where proteins associate in the plane parallel to the β sheet. The homodimer interface involves residues strongly conserved in the D (type II) Prxs, suggesting that all Prxs of this family can homodimerize. The study provides a new insight into the Prx oligomerism and the basis for protein—protein and enzyme—substrate interaction studies by NMR.

Peroxiredoxins (Prxs)[1] are thiol-specific antioxidant proteins that catalyze the reduction of hydrogen peroxide, peroxinitrite, and hydroperoxides, some of the reactive oxygen species responsible for oxidation and degradation of lipids, nucleic acids, and proteins. The first Prx was discovered in 1988 as a yeast antioxidant protein devoid of a prosthetic group and selenium (*1*). Since then, the number of identified Prxs has increased steadily, and heterologues have been found in bacteria to humans with several isoforms

† This work was supported by grants from CNRS (GDR "Thiorédox" 2477) and financial support from the French Ministère de l'Education Nationale, de la Recherche et des Technologies to A.E., X.T., and N.R.

* To whom correspondence should be addressed: RMN Biomoléculaire, Université Claude Bernard—Lyon1, Domaine Scientifique de la Doua, ESCPE-Lyon, F-69622 Villeurbanne Cedex, France. Telephone/Fax: (+33) 4 72 43 13 95. E-mail: isabelle@hikari.cpe.fr (I.K.); Telephone/Fax: (+33) 4 72 43 13 95. E-mail: lancelin@hikari.cpe.fr (J.-M.L.).

‡ LCM3B, Groupe Biocristallographie.

§ A.E. and X.T. have contributed equally.

|| UMR CNRS 5180 Sciences Analytiques.

⊥ UMR Interaction Arbres Microorganismes.

[1] Abbreviations: AhpD, alkyl hydroperoxide reductase D; AhpF, alkyl hydroperoxide reductase flavoprotein; BMRB, BioMagResBank; Grx, glutaredoxin; MW, molecular weight; NMR, nuclear magnetic resonance; NOE, nuclear Overhauser effect; PDB, Protein Data Bank; PEG, poly(ethylene glycol); Prx, peroxiredoxin; R_1, longitudinal relaxation rate; R_2, transversal relaxation rate; Trx, thioredoxin.

10.1021/bi048226s CCC: $30.25 © 2005 American Chemical Society
Published on Web 01/15/2005

Table 1: Structures of Prxs

Prx name	subfamily	PDB code	source	redox state	oligomeric state	resolution (Å)	residues observed
rPrxI	A	1QQ2	*Rattus norvegicus*	C−SS−C	α_2	2.6	3−175
hPrxII	A	1QMV	*Homo sapiens*	C−SO_2^-	$(\alpha_2)_5$	2.7	1−198
TryP	A	1E2Y	*Crithidia fasciculata*	C−SH	$(\alpha_2)_5$	3.2	6−166
AhpC	A	1H4O	*Salmonella typhimurium*	C−SS−C	$(\alpha_2)_5$	2.5	1−165
AhpC	A	1NJ8	*Salmonella typhimurium*	C−SH	$(\alpha_2)_5$	2.2	1−186
hPrxVI	B	1PRX	*Homo sapiens*	C−SOH	α_2	2.0	2−224
hPrxV	D	1HD2	*Homo sapiens*	C−SH	α_2	1.5	1−161
hPrxV	D	1OC3	*Homo sapiens*	C−SS−C	α_2	1.5	1−161
PrxV hybrid	D	1NM3	*Haemophilus influenzae*	C−SH	α_2	2.8	3−239
*Ec*TPx	E	1QXH	*Escherichia coli*	C−SS−C	α_2	2.2	2−165
*Sp*TPx	E	1PSQ	*Streptococcus pneumoniae*	C−SH	α_2	2.3	1−163
*Hi*TPx	E	1Q98	*Haemophilus influenzae*	C−SS−C	α_2	1.9	2−165
this study	D	1TP69	*Populus trichocarpa*	C−SH	α_2	1.6	2−162

in all organisms (*2*−*5*). Prx functions are still far from being understood, and their catalytic efficiency is somewhat low, about 10^5 M^{-1} s^{-1} (*2*, *3*). Common features of Prxs include the presence of one strictly conserved catalytic cysteine, called the peroxidatic cysteine, located in the N-terminal part of an α helix, together with a proline, an arginine, and a hydroxylated residue conserved in the active site. The peroxidatic cysteine, after reacting with the hydroperoxide, is oxidized into a sulfenic acid Cys-SOH (*6*, *7*). The oxidized Prx is then regenerated by a thiol-containing substrate. Three mechanistic groups (1-Cys, 2-Cys, and atypical 2-Cys Prxs) have been identified, according to the catalytic steps following the sulfenic acid formation. In 1-Cys Prxs, the sulfenic acid was shown to be directly reduced by a reductant, such as glutathione, lipoic acid, or cyclophilin (*8*−*10*), whereas in 2-Cys Prxs, the sulfenic acid reacts with a second conserved cysteine of another subunit, called the resolving cysteine, to form an intermolecular disulfide bridge. The disulfide is then reduced by a disulfide oxidoreductase [thioredoxin (Trx) (*11*), tryparedoxin (*12*), alkyl hydroperoxide reductase D (AhpD) (*13*), alkyl hydroperoxide reductase flavoprotein (AhpF) (*14*), or glutathione (*15*)]. The third mechanistic group of Prxs is the atypical 2-Cys Prx group, in which the disulfide is formed between the sulfenic acid and a second cysteine located in the same peptidic subunit. This intramolecular disulfide is reduced by disulfide oxidoreductases such as Trxs (*16*).

The structural events linked to the Prx catalytic mechanism have been highlighted by the resolution of Prx 3D structures in various redox states (Table 1). The typical 2-Cys Prx mechanism is particularly well-documented (*2*, *17*−*20*). Briefly, the peroxidatic sulfenic acid of 2-Cys Prxs is located in the first turn of an α helix that unwinds to form a disulfide bridge with the C-terminal resolving cysteine of another subunit. The disulfide is reduced, and the peroxidatic cysteine loop returns to a helical conformation. Structural data are scarce for atypical 2-Cys Prxs. Resolution of the human PrxV structure in the reduced state has shown that formation of the intramolecular disulfide requires a conformational change, because the two cysteines, which are separated by ca. 100 amino acids, are more than 13.8 Å apart (*21*, *22*). Recently, the structure of an atypical 2-Cys Prx from *Escherichia coli* (TPx) has been resolved in the oxidized state (*23*). Together with the modeling of the reduced form, the crystal structure suggests that the two loops containing the peroxidatic and resolving cysteines likely undergo a conformational change upon oxidation similar to the one making the disulfide formation possible in 2-Cys Prxs (*23*).

From the comparison of the peptidic sequences, Prxs appear as a very diverse family of proteins and can be classified into five subfamilies named A, B, C, D, and E (*3*, *24*). In plants, four groups are found (*4*, *5*). Exemplified by Prxs with solved 3D structures, A Prxs encompass proteins homologous to human PrxII (*19*) and rat PrxI (*18*) 2-Cys Prxs, whereas B Prxs are homologous to human PrxVI 1-Cys Prx (*7*). C Prxs include bacterioferritin comigratory proteins and PrxQs found in bacteria and plants and are characterized by an active-site sequence CXXXXC (*25*, *26*). No structures of this subfamily have been solved. D Prxs are homologous to yeast type II Ahp1 (*24*, *27*−*29*) and include human PrxV (*21*, *22*) and hybrid PrxV (*30*) from *Haemophilus influenzae*. Finally, E Prxs consist of bacterial Prxs only, named thiol peroxidases (TPx), with the recently solved structure of *E. coli* TPx (*23*).

The oligomeric state of Prxs is intensively investigated. The oligomeric properties in solution of A Prxs (typical 2-Cys Prxs) are mainly linked to the redox state of the proteins, the ionic strength, and the pH (*2*). Structural studies have shown that A Prxs are decamers in the reduced and over-oxidized (sulfinate) redox states, whereas they are homodimers in the oxidized state (*2*, *17*, *19*, *20*). B and E Prxs are thought to be homodimers, according to their crystallographic structures (*7*, *23*). The oligomerism of D (type II) Prxs including the human PrxV is unclear from the literature (*21*, *22*, *27*, *30*). Atomic resolution studies are necessary for a precise knowledge of the enzyme oligomeric state in solution. This is essential in the context of the numerous protein−protein interactions in which Prxs are involved.

To gain insight into the oligomerism of D (type II) Prxs and to understand the glutaredoxin (Grx) dependence, we have undertaken a combined X-ray and solution nuclear magnetic resonance (NMR) study of a plant Prx from *Populus*, member of the D (type II) Prxs (*27*, *24*, *31*). The poplar Prx possesses two cysteines, but mutagenesis studies have shown that only one cysteine is necessary for the catalytic cycle (*31*, *32*). The plant Prx is the first Prx shown to be regenerated *in vitro* by both Grx and Trx systems (31). Since then, other plant D Prxs have been shown to be reduced by Grx only (*33*), and fusion proteins containing both Prx and Grx domains in the same sequence have been found in pathogenic bacteria (*23*, *34*−*36*). For the first time, the combination of the crystal structure and the solution NMR dynamics provides evidence of a conserved homodimeric state of the reduced Prx in the crystal and in solution. We show that the Prx−Prx interface involves a surface perpen-

dicular to the central β sheet with conserved interfacial residues, which suggests that all D (type II) Prxs could homodimerize. Such an interface has been also characterized in E Prxs (*30*) but is very different from the interaction surface of A- and B-Prx dimers, which is parallel to the β sheet (*2*, *7*). The two types of Prx−Prx interfaces described so far for the different Prx oligomeric states are discussed in the global structure and also at the interaction level.

EXPERIMENTAL PROCEDURES

Expression and Purification of D (Type II) Poplar Prx. Samples for crystallization were produced as previously described (*37*). NMR samples were prepared from 0.08 to 0.8 mM, 50 mM phosphate buffer at pH 7.2, as previously described (*38*).

Crystallization, Data Collection, Structure Determination, and Refinement. Crystallization conditions of the poplar Prx have been described previously (*37*). Briefly, monoclinic crystals were obtained in the presence of 30% poly(ethylene glycol) (PEG) molecular weight (MW) 4000, 0.1 M Tris-HCl at pH 8.0, and 0.2 M Li_2SO_4 at a protein concentration of 15.6 mg/mL. A complete native data set was collected on beam line DW32 at the LURE (λ = 0.948 Å, Orsay, France). Crystals belong to space group $P2_1$ with unit cell parameters a = 59.26 Å, b = 68.80 Å, c = 75.71 Å, and β = 93.45° and contain 4 molecules per asymmetric unit. They diffracted to 1.62 Å, with data completeness and $I/\sigma(I)$ of 95.8 and 15%, respectively, overall, and 83.5 and 4% for the 1.68−1.62 Å shell (*37*). Using the coordinates of human PrxV (PDB entry 1HD2) as a search model, a molecular replacement solution was found for a V152C mutant Prx, for which triclinic crystals contain only 2 molecules per asymmetric unit (*37*). Several cycles of refinement alternated with manual rebuilding were carried out to improve this first model. Regions 19−25 and 110−127 were not defined in the electron density maps. The structure of the partially rebuilt V152C monomer has then been used as a molecular replacement template for the wild-type structure. Arp/wArp was used in molrep mode to refine the positions of the molecules obtained in first instance by molecular replacement and then in automatic rebuilding mode. Cycles of refinement (CNS) (*39*) alternated with manual rebuilding (TURBO−FRODO) (*40*) and inclusion of higher resolution data were carried out to improve the models. A total of 10% of the data was set aside for R_{free} calculations. Water molecules were added automatically using the automated procedure implemented in CNS suite and checked manually. Their positions were kept only where interactions were favorable and where the ($F_o - F_c$) difference Fourier map showed a density of more than 3.0 σ. Some residues (regions 17−27 and 143−148) were badly defined and needed to be rebuilt manually. The last refinement steps were carried out using Refmac5 (*41*) with the geometrical weighting term set to 0.5. The final R factors values for the working (R) and the test (R_{free}) sets are 18.9 and 22.4%, respectively, and the figure of merit reaches 86.1% at the last step.

Structure Analysis and Final Structure Parameters. The final model contains residues 1−162 in molecules A, B, and C, residues 1−160 in molecule D, 623 water molecules, and 2 sulfate ions. The stereochemical analysis was carried out with Procheck (*42*) and highlighted 471 nonglycine residues in the most favored area, 77 residues in the additional allowed area, 1 residue in the generously allowed area, and none in the disallowed area. The coordinates and the structure factors have been deposited in the Protein Data Bank (PDB) at Research Collaboratory for Structural Bioinformatics (PDB entry 1TP69).

NMR Relaxation Measurements. All relaxation experiments were performed with a 0.8 mM protein sample at 500 MHz and 38 °C. R_1 (longitudinal relaxation rate), R_2 (transverse relaxation rate), and the steady-state ^{1}H-^{15}N nuclear Overhauser effect (NOE) measurements were performed using the usual pulse sequences (*43*) and in identical experimental conditions used for yeast Ahp1 Prx (*24*). The R_1 and R_2 experiments were collected with 130 complex t1 increments, 1024 t2 points, and 48 scans for each FID. For R_1 measurements, spectra were recorded with six inversion recovery delays of 22, 55, 155 (twice), 255, 500, and 755 ms. For R_2 measurements, spectra were recorded at five Carr−Purcell−Meiboom−Gill (CPMG) delays of 17, 33, 50, 67, and 83 ms and spectra were duplicated at 33 and 67 ms. A total of 900 ms separated two 180° ^{15}N pulses in the CPMG sequence. ^{1}H-^{15}N NOE spectra with 130 complex t1 increments, 1024 t2 points, and 304 scans per FID were recorded in an interleaved way with and without proton saturation during relaxation delay. Recycle delays of 5 and 2 s were used for the spectrum recorded respectively in the absence and occurrence of proton saturation. The ^{1}H saturation was achieved by the application of 120° ^{1}H pulses separated by 5 ms, for a period of 3 s.

Rotation Diffusion Analysis. The rotational diffusion tensor of the protein was derived from the orientation dependence of

$$\left(\frac{2R_2'}{R_1'} - 1\right)^{-1} = \frac{3}{4}\frac{J(\omega_N)}{J(0)} \qquad (1)$$

The primes in R_2' and R_1' indicate that these relaxation rates were modified to subtract the contributions from high-frequency components of the spectral density as described in previous papers (*44*−*46*). The advantage of using the ratio, R_2'/R_1', instead of the individual values of these parameters is that this ratio is independent, to a first approximation, of the site-specific variations in the strength of ^{1}H-^{15}N dipolar coupling and ^{15}N chemical-shift anisotropy. Moreover, in the case of protein core residues, the R_2'/R_1' ratio primarily depends on the overall tumbling and is practically insensitive to fast, subnanosecond backbone dynamics, because the order parameters of local motions in the numerator and the denominator of eq 1 cancel out (*47*). In the present study, 66 residues in well-ordered secondary structure element with NOE > 0.7 were used to derive rotational diffusion characteristics. The crystal structure of the mono- and homodimeric protein were protonated using Molmol (*48*), whereas optimization of the rotational diffusion tensor against experimental data was performed by using ROTDIFF (*49*).

Hydrodynamic Calculations. Theoretical prediction of the rotational properties of proteins in solution is complex. Indeed, it has to account for the size and shape of the protein under study as well as the hydration shell formed by water molecules moving together with the tumbling protein. We used here the "shell modeling" strategy from Garcia de la Torre implemented in the HYDRONMR software (*50*). The

latter approach is characterized by a single parameter *a*, the atomic element radius that represents the sum of the thickness of the hydration shell and the average van der Waals radius in the molecule. Nevertheless, the choice of the *a* parameter is a critical point and needs to be optimized against the experimental relaxation data. The procedure described by Bernado and colleagues is based on the insensitivity of the T_1/T_2 values over all of the residues, namely, ∇_i (*51*). Here, we found that the relative deviations of the ρ factor over all residues are already insensitive (data not shown). As a consequence, the complete algorithm to select the optimal *a* value has been implemented in Matlab (The MathWorks, Inc.) for a set of 20 values ranging from 2 to 4 Å. All of the calculations were performed by using the viscosity of water at 37 °C, $\eta = 0.667$ Ns/m^2. A first estimate of the atomic element radius was obtained and then refined a second time to give rise to a best value of 3.22 Å. The latter value is in good agreement with the average *a* value (e.g., 3.3 Å) determined previously by Bernado et al. on a set of 15 different proteins (*51*).

Modeling. A dimeric form of the poplar Prx in which the monomers associate in the plane parallel to the β sheet was calculated using Modeller (*52*). The model was used to analyze the relaxation data. The structure of the dimer found in the decamer of the AhpC A-Prx protein was used as a template (PDB entry 1N8J).

RESULTS AND DISCUSSION

Crystal Structure. The crystal structure of poplar D Prx has been resolved at 1.6 Å resolution in the reduced state (Figure 1 and Table 2). The crystal contains four molecules per asymmetric unit without any direct angular relationships. Three of the four molecules (called A, B, and C) interact together, while the fourth molecule (D) is separated by a solvent channel. The strongest contacts are found between molecules A and B and involve two salt bridges ($E61_A-K54_B$ and $K62_A$ and $E156_B$) and several hydrogen bonds between residues at position 65−68 (helix α3) in molecule A and residues 156−160 (helix α5) from molecule B. Another salt bridge ($E94_B-K54_C$) and one hydrogen bond participate in the interaction between molecules B and C, while the AC interface involves one hydrogen bond only. No significant structural differences are observed between the four molecules, with the mean root-mean-square (rms) values varying from 0.25 to 0.59 Å for the Cα atoms. For molecules A, B, and C, the mean rms values vary from 0.25 to 0.33 Å and the main structural difference concerns the orientation of the N-terminal $\beta1-\beta2$ region relative to the protein core. The superimposition of molecules A, B, and C on molecule D shows a higher rms deviation (rmsd) close to 0.6 Å. In addition to the N- and C-terminal extremities, the solvent-exposed loop $\beta1-\beta2$ and the region 56−68 from helix α2 in close vicinity to the C terminus do not superimpose very well with the three other molecules. The lack of interactions between molecule D and the three other molecules of the asymmetric unit can partially account for these conformational differences.

To date, 12 crystal structures of Prxs have been solved in various redox and diverse oligomeric states (Table 1). The superimposition of the poplar Prx structure with other Prx structures from different subfamilies (A, B, and E Prxs) shows a conserved fold of the protein core and more precisely of the Trx fold (Figure 1). The Trx fold is completed by one α helix and three β strands in the poplar Prx, forming a seven-stranded central β sheet surrounded by five α helices

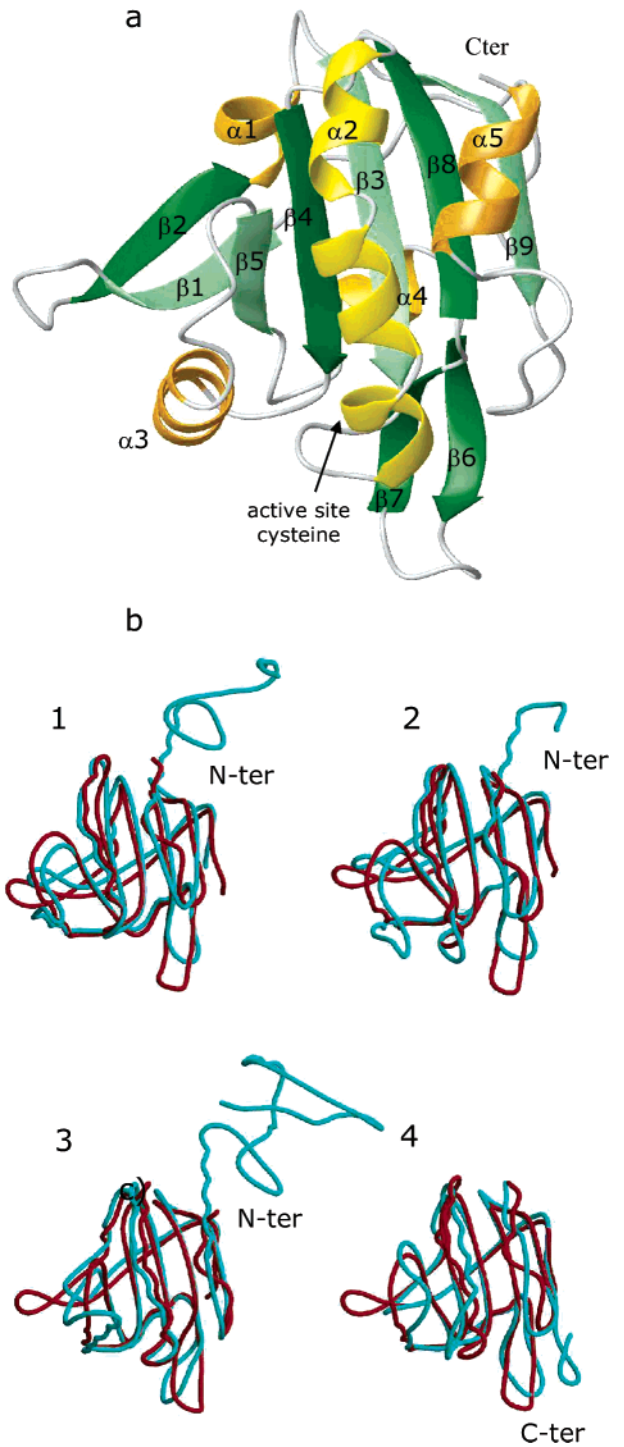

FIGURE 1: Structure of the monomer (molecule A of the asymmetric unit) of the poplar Prx and superimposition based on the Cα atoms of poplar Prx with Prxs of different subfamilies. (a) Structure of the poplar Prx is shown in a ribbon representation. (b) Structure of the poplar Prx (in red) is superimposed on the structures of different Prxs (in cyan). (1) Superposition with A Prx from *Homo sapiens* [hPrxII (*19*), PDB entry 1QMV]. (2) Superposition with A Prx from *Rattus norvegicus* [rPrxI (*18*), PDB entry 1QQ2], (3) Superposition with B Prx from *H. sapiens* [hPrxVI (*7*), PDB entry 1PRX]. 4) Superposition with E Prx from *E. coli* [EcTPx (*23*), PDB entry 1QXH]. The ribbon representation was done with Molmol (*48*) and the superimposition was done with lsqab (*59*).

Table 2: Data Collection and Refinement Statistics

data collection	
space group	$P2_1$
unit cell (Å, deg)	$a = 59.26$, $b = 68.80$, $c = 75.71$, $\beta = 93.45$
Z	8
nominal resolution (Å)	19.88−1.62
outermost resolution shell (Å)	1.68−1.62
unique reflections	79 011
completeness (%)	95.8 (83.5)[a]
mean $I/\sigma(I)$	15 (4)[a]
R_{merge} (%)[b]	6.2 (19.0)[a]
refinement statistics	
R factor (%)[c]	18.9
R_{free} (%)[d]	22.4
rmsd from ideal geometry	
bond lengths (Å)	0.020
angles (deg)	1.79
dihedral angles (deg)	23.3
improper angles (deg)	0.82
average B factor (Å^2)	
protein atoms (main chains/side chains)	22.25 (20.9/23.65)
sulfate anions	37.0
water molecules	29.3

[a] Values in parentheses refer to the outermost resolution shell. [b] R factor for symmetry-related intensities. [c] Crystallographic R factor. [d] R factor for a randomly selected 10% reflections not included in refinement.

(Figure 1). An independent two-stranded β sheet ($\beta6-\beta7$) is found in the loop connecting helix α4 and strand $\beta8$ (Figure 1). This loop is a region of the protein that presents variable structures in Prxs: α helix in human PrxV (*21*), β hairpin in hybrid PrxV or A Prxs (*19*, *20*, *30*), or a noncanonical structure (*7*, *18*). The rmsd values from the superimpositions of poplar Prx with A Prxs [rPrxI (*18*) and hPrxII (*19*)], B Prx [hPrxVI (*7*)], and E Prx [EcTPx (*23*)] are between 1.5 and 1.6 Å for 107, 111, 109, and 94 Cα atoms, respectively (Figure 1). Apart from the loop conformation differences, the topology differences reside mainly in the C-terminal extension and in the presence of an additional α helix (residues 93−97 using poplar Prx numbering) for A and B Prxs and in a N-terminal extension for E Prx (Figure 1). Two structures of D Prxs have been determined in addition to the poplar Prx: the human PrxV (*21*, *22*) and the Prx domain of hybrid PrxV (*30*) that share 42.4 and 36.5% of sequence identity with the poplar Prx, respectively. Accordingly, the crystal structures are very similar and superimpose with a rmsd of 1.0 and 1.1 Å, respectively. Therefore, the redox dependence to Trx and Grx should be due to the proper surface interaction driven by amino acid side chains (see below, the Prx−Grx Interaction).

NMR Assignments. We have recently reported the NMR assignment of the poplar Prx obtained with a ^{15}N, ^{13}C, 50% ^{2}H labeled sample [BioMagResBank (BMRB) entry 6132] (*38*). Together with the secondary chemical shifts of the backbone atoms, NOE correlations and hydrogen-exchange experiments enabled to check that the solution structure is similar to the crystal structure. Moreover, Φ and Ψ backbone angles predicted from the NMR assignments by Talos (*53*) for the protein in solution are similar to the angles in the crystal except for four residues (P49, D103, T151, and S153).

Active Site. The active site is roughly divided into two parts. The first part, exposed to the solvent, is polar and positively charged, whereas the second part is more hydrophobic (residues 41−47, 56−60, and 88). The position of the catalytic cysteine C51 allows side-chain interactions with R129, a residue strictly conserved among Prxs (distance of R129 N^{ϵ}−C51 S^{γ}, 3.3 Å), and T48 (distance of C51 S^{γ}−T48 O^{γ}, 3.2 Å) (Figure 2). A water molecule (wat289) might also interact with the C51 S^{γ} atom at a distance of 3.4 Å. A sulfate molecule is present in the active site of molecules A and B of poplar Prx (Figure 2). This sulfate anion is stabilized by interactions with T50 and K121 and with a water molecule. T48V and R129Q mutants of the poplar Prx have shown that both residues are necessary for the reduction of substrates such as the hydrogen peroxide and tertiary butyl hydroperoxide but not for the degradation of cumyl hydro-

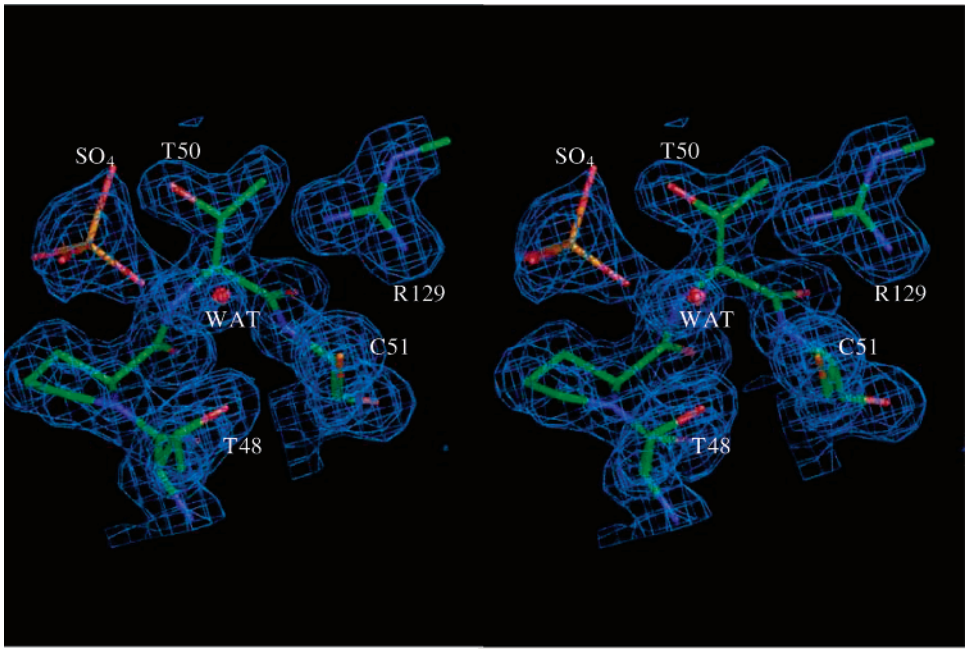

FIGURE 2: Stereoview of selected amino acids in the poplar Prx active site in the ($2f_0 - f_c$) electron density map (contour level of 1.0 σ).

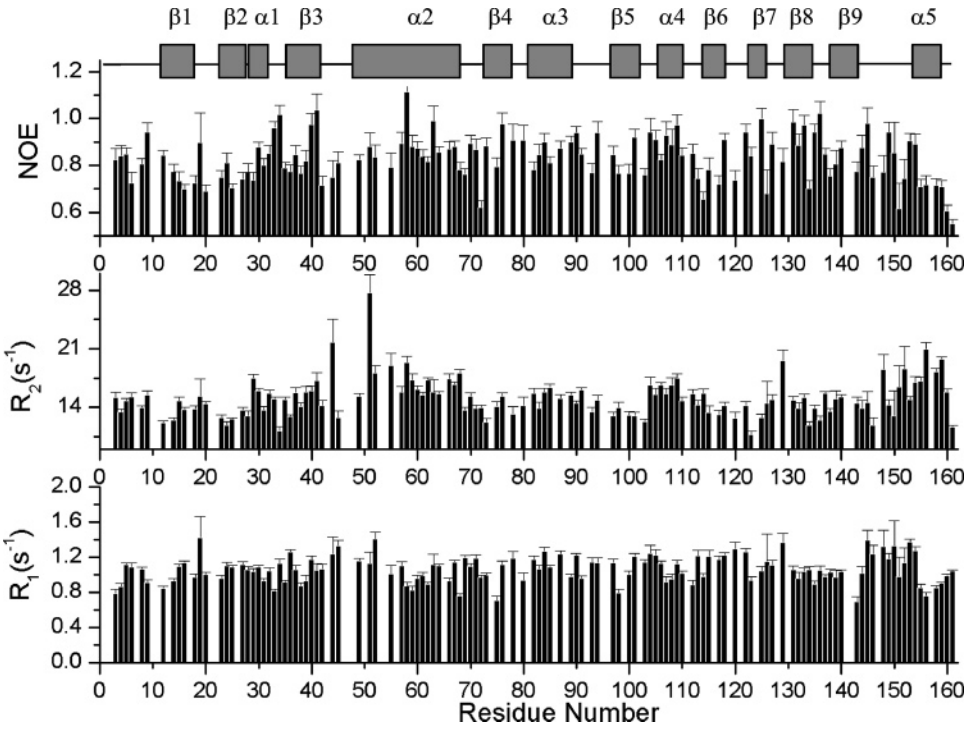

FIGURE 3: Reduced poplar Prx ^{15}N-relaxation parameters R_1, R_2, and ^{15}N $\{^1$H$\}$ NOE versus the residue number. The error bars represent standard deviations in the estimated parameters.

peroxide (*54*). This suggests that the mutations affect the active-site structure but not the thiol-dependent regeneration of the enzyme (*54*).

The catalytic cysteine of poplar Prx is reduced in the crystal. However, no reducing agents have been used to grow the crystals, suggesting a low sensitivity of the cysteine to auto-oxidation. Such a behavior of the enzyme has already been observed in the protein production steps (*31*). In the human PrxVI structure (B Prx), the catalytic cysteine is oxidized into a sulfenic acid. A histidine residue (H39), together with the putative presence of a Mg^{2+} ion, was proposed to stabilize the sulfenic acid and to prevent over-oxidation (*7*). The active site of the poplar Prx also contains a histidine residue (H55), but the histidine is not as close to the cysteine as in B Prxs. The neutral histidine H55 is involved in a hydrogen-bonding network with Nη1−Hη12 of the invariant arginine (R129) and with the S153 carbonyl. This network is also found in human PrxV and hybrid PrxV structures.

Oligomerization of the Poplar D Prx. NMR relaxation data are sensitive to the overall reorientation of proteins in solution and to the protein local dynamics and can therefore provide valuable information regarding the oligomerization state of proteins. ^{15}N R_1, R_2, and ^{1}H-^{15}N NOE relaxation data were recorded on a uniformly ^{15}N-labeled sample of the poplar Prx at 38 °C and ^{1}H = 500 MHz. The relaxation data are shown in Figure 3. The poplar Prx is overall well-structured from the N to C terminus and does not present strongly disordered regions correlating with X-ray diffration that gave a set of electronic densities for all residues. The mean value for the ^{15}N R_1 and R_2 are 1.08 ± 0.15 and 15.1 ± 2.3 s^{-1}, respectively. It is noteworthy that both values are significantly different from expected for a monomeric protein of ca. 18 kDa (*55*). The experimental overall reorientational tumbling calculated from the relaxation data (14.0 ns) is much larger than expected for a monomeric protein, as deduced from the Stokes−Einstein relation (5.35 ns for a nonhydrated protein and 8.38 ns if a 3.2 Å water layer is included). The slower overall rotation of the poplar Prx could be due to a protein dimerization in solution. In the crystal, even though a dimer is not found in the asymmetric unit (see above), reconstruction of the crystal lattice reveals a significant dimeric association involving a protein surface perpendicular to the β sheet (see below). Then, to analyze the NMR relaxation data, both dimeric and monomeric forms of the poplar Prx were used as structural models.

The rotational diffusion tensor orientation was accurately determined with respect to the protein inertial tensor for the mono- and dimeric Prx (Table 3). On the basis of the ratios of the principal components of the inertia tensor (1.00:0.99:0.34), the homodimeric protein is expected to have a substantially anisotropic diffusion tensor. The isotropic, axially anisotropic, and fully anisotropic models of rotational tumbling satisfy the experimental data. However, the fit improvement achieved with the fully anisotropic model is not statistically significant, as determined by a F test (p = 0.065). The axially symmetric model agrees with the experimental relaxation data significantly better than the isotropic model (Table 3), as determined by a F test (p = 7.23×10^{-15}). Moreover, the orientations of the diffusion and inertia tensor z principal axis nearly coincide with an angle difference of 2.13° (Figure 4a). The axially symmetric model is characterized by $D_{\parallel/\perp}$ = 1.60 ± 0.05 and τ_c = 14.11 ± 0.40 ns, with the principal axis orientation with respect to the crystal structure defined by α = 21 ± 5° and β = 103 ± 5° (Figure 4a). If the crystallographic monomeric model of the Prx is used, the relaxation data are no longer consistent with the overall correlation time τ_c (Table 3). In addition, the angle difference between the diffusion and inertia tensors is 18.1° (Figure 4b). These relaxation data

Table 3: Rotational Diffusion Tensor Parameters for the Poplar Prx

Monomer (X-ray Structure)

model	D_x (10^7 s^{-1})	D_y (10^7 s^{-1})	D_z (10^7 s^{-1})	α[a]	β[a]	γ[a]	τ_c[b]	anisotropy[c]	rhombicity[d]	χ^2/df[e]	*P*[f]
isotropic	1.16 ± 0.01	1.16 ± 0.01	1.16 ± 0.01				14.33 ± 0.10	1	0	15.32	
axially symmetric	0.99 ± 0.04	0.99 ± 0.04	1.59 ± 0.04	13 ± 7	108 ± 7		14.04 ± 0.60	1.61 ± 0.07	0	9.17	2.57×10^{-8}
fully anysotropic	0.91 ± 0.10	1.08 ± 0.10	1.57 ± 0.15	10 ± 8	106 ± 9	159 ± 30	14.02 ± 0.80	1.58 ± 0.20	0.437 ± 0.080	8.9	10.1×10^{-2}
theoretical prediction[g]	2.53	2.77	2.83	15.9	118.9	170.0	6.15				

Dimer (X-ray Structure)

model	D_x (10^7 s^{-1})	D_y (10^7 s^{-1})	D_z (10^7 s^{-1})	α[a]	β[a]	γ[a]	τ_c[b]	anisotropy[c]	rhombicity[d]	χ^2/df[e]	*P*[f]
isotropic	1.16 ± 0.01	1.16 ± 0.01	1.16 ± 0.01				14.33 ± 0.12	1	0	14.5	
axially symmetric	0.99 ± 0.03	0.99 ± 0.03	1.57 ± 0.06	21 ± 5	103 ± 5		14.11 ± 0.40	1.60 ± 0.05	0	8.15	7.23×10^{-15}
fully anysotropic	0.91 ± 0.07	1.07 ± 0.08	1.57 ± 0.12	21 ± 7	102 ± 6	27 ± 23	14.08 ± 0.65	1.59 ± 0.15	0.393 ± 0.059	7.93	6.5×10^{-2}
theoretical prediction[g]	0.957	0.959	1.624	21.8	105.2	−10.1	14.12	1.69	4.5×10^{-3}		

Dimer (Model Homologous to AhpC Dimer)

model	D_x (10^7 s^{-1})	D_y (10^7 s^{-1})	D_z (10^7 s^{-1})	α[a]	β[a]	γ[a]	τ_c[b]	anisotropy[c]	rhombicity[d]	χ^2/df[e]	*P*[f]
isotropic	1.16 ± 0.01	1.16 ± 0.01	1.16 ± 0.01				14.33 ± 0.17	1	0	19.45	
axially symmetric	1.03 ± 0.04	1.03 ± 0.04	1.41 ± 0.11	100 ± 14	127 ± 25	14.42 ± 0.71		1.36 ± 0.10	0	14.46	1.16×10^{-6}
fully anysotropic	0.98 ± 0.13	1.09 ± 0.13	1.41 ± 0.16	99 ± 28	128 ± 18	59 ± 40	14.38 ± 0.90	1.37 ± 0.20	0.417 ± 0.140	14.23	4.88×10^{-1}
theoretical prediction[g]	0.99	1.017	1.643	80.1	127.3	95	13.66	1.63	4.7×10^{-3}		

[a] Euler angles {α,β,γ} (in degrees) describe the orientation of the principal axes frame of the rotational diffusion tensor with respect to the protein coordinate frame. [b] Overall rotational correlation time (in nanoseconds) of the molecule. [c] The degree of anisotropy of the diffusion tensor, $2D_z/(D_x + D_y)$. [d] The rhombicity of the diffusion tensor, $1.5(D_y - D_x)/[D_z - {}^1/_2(D_x + D_y)]$. [e] Residuals of the fit (χ^2) divided by the number of degrees of freedom. [f] Probability that the reduction in χ^2 (compared to the model in the above row) could occur by chance. [g] The results of hydrodynamic calculations using HYDRONMR. The parameter *a* was set to 3.22 Å.

strongly support that the crystal homodimer of the Prx is conserved in solution *in vitro*.

Hydrodynamic Calculations. The Stokes−Einstein equation gives only a rough estimate of the molecular tumbling in solution. To account for a better estimate of the protein shape, we performed hydrodynamic calculations using HYDRONMR (*50*). Correlation times of 6.15 and 14.12 ns were obtained for the mono- and dimeric states of the Prx, respectively. These results clearly account for a homodimeric structure of the Prxs in solution. Beside the fact that the theoretical prediction of the diffusion tensor orientation for the homodimer nearly coincides with the inertia tensor (1° tilted), calculations were able to reproduce the relaxation data pattern along the residue number (Figure 5). Nevertheless, we can notice an opposite profile of the calculated and experimental data spanning residues 114−125 corresponding to the β6−β7 region. Such a behavior could account for a discrepancy between the NH vector orientation in the crystal structure and in solution.

Prx−Prx Interface of D Prxs. The dimer interface of the poplar Prx in the crystal involves nine residues located in loop β3−α2, turn β4−α3, helix α3, and loop α4−β8 (Figure 6). The interface buries 742 Å^2 per monomer and is mainly stabilized by hydrophobic interactions in addition to charge interactions through two salt bridges. Residues T48, P49, and L123 from one monomer interact with F83 of the other monomer, and F47 has van der Waals contacts with residues A87 and V84 (Figure 6). The electrostatic interactions involve residues D81 of one monomer and R126 of the other monomer. Residues F47, T48, and P49 belong to loop β3−α2; D81 is part of turn β4−α3; F83, V84, and A87 are helix-α3 residues; and L123 and R126 are residues of loop α4−β8. Six intermolecular hydrogen bonds are observed between S105 H^{γ} and Q119 O, G124 H^N and S105 O^{γ}, and R126 H^{η} and D81 O^{δ}.

The dimer is very different from the dimer of typical 2-Cys and 1-Cys Prxs (A and B Prxs) (see below). However, a homologous dimer was reported for *H. influenzae* hybrid PrxV (D Prx), which contains an attached Grx domain (*30*). This suggests that the dimeric form is conserved upon the interaction of the poplar Prx with Grx.

Even though the homologous human PrxV was reported as a monomer in the crystal structure (*21*), the same Prx−Prx interactions are found by analysis of the crystal lattice (*30*). The residues involved in the interface are conserved in the human *H. influenzae* and poplar D Prxs, except for L123, which is replaced in the hybrid PrxV and the human PrxV by hydrophobic residues (Figure 7). The Prx−Prx interfaces in the three Prxs are roughly perpendicular to the plane of the central β sheet (Figure 6) and are completely different from the dimer interface in A and B Prxs, where proteins associate in the plane parallel to the β sheet (Figure 8) (*2*, *7*, *17*−*20*).

To show that the relaxation data provide evidence that the homodimer in solution corresponds to the homodimer found in the crystal, we have modeled a homodimer homologous to the AhpC A Prx (*20*). In this model, the Prx−Prx interaction surface is no longer perpendicular to the β sheet

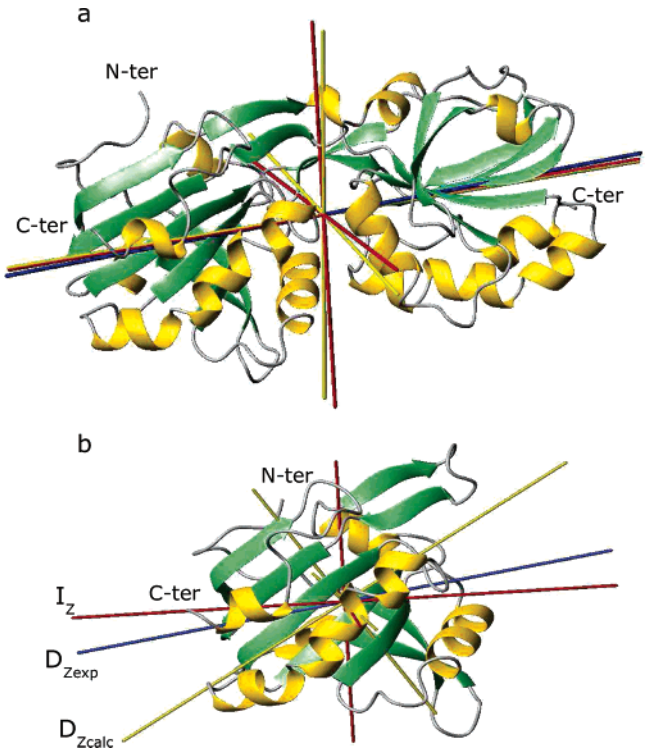

FIGURE 4: Rotational diffusion tensor orientation of the homodimeric (a) and monomeric (b) forms of the poplar Prx generated using Molmol (*48*). Rods represent the rotational diffusion axes derived from relaxation data (blue, $D_{z,exp}$), the inertial tensor axes (red, I_z), and the theoretical rotational diffusion axes (yellow, $D_{z,calc}$). For the homodimeric structure (a), the *z* axis of the diffusion tensor makes an angle of 2.13° with the corresponding inertia axis, whereas it is tilted 2.31° from the theoretical diffusion axis. For the monomeric structure (b), the *z* axis of the diffusion tensor is tilted 18.1° from *z* axis of the inertia tensor, whereas a difference of 24.3° is observed with the theoretical diffusion tensor orientation.

but parallel to the β sheet, as observed in the dimer of the AhpC A Prx (Figure 8a). The relaxation data were analyzed using this new model (Table 3 and Figure 5). In this case, the axially symmetric model still prevails with a lower anisotropy of 1.36 ± 0.1. However, the residual of the fit divided by the number of degrees of freedom exhibits a higher value (14.46) compared to the value obtained when relaxation data are fitted against the "perpendicular" homodimeric model of the protein (9.17). Furthermore, the orientation of the *z* diffusion axis is substantially tilted about 80° from the *z* inertia axis, and the space-sampling parameter (*56*) is not as relevant (0.011) as for the perpendicular model (0.007). Hydrodynamic calculations were performed for this model and gave rise to a large discrepancy between the predicted and experimental relaxation data (Figure 5). At this stage, NMR discriminates unambiguously the dimer type of the poplar Prx in solution.

Ahp1 (yeast D Prx) has been shown by analytical ultracentrifugation to be dimeric in solution independently of the redox state (*24*). NMR relaxation data for reduced Ahp1 were similar to the poplar Prx, with average R_1 and R_2 values in secondary structure elements of 0.81 ± 0.08 and 19.7 ± 1.9 s^{-1}, respectively (*24*). Because no structures of Ahp1 are available, models of a monomer and dimer were calculated with Modeller (*52*), using the crystal structure of the hybrid PrxV (*30*). Relaxation data analyzed with the models clearly show that Ahp1 is a homodimer with an interface perpendicular to the β sheet (data not shown). NMR relaxation experiments were also recorded for another D Prx from *Arabidopsis thaliana* (AtPrxII-E) in the reduced state. Even if the NMR signals were not assigned, the average R_1 and R_2 relaxation rate values (0.81 ± 0.08 and 20.6 ± 2.0 s^{-1}, respectively) suggest that the protein is also a dimer in solution (data not shown).

We have previously analyzed 60 peptidic sequences of the D-Prx subfamily (*24*). Residues F47, T48, and P49 involved in the interface are strictly conserved in all sequences except for two mitochondrial Prxs (YTG) and yeast Ahp1 (FSP). In general, D81 is strictly conserved but is replaced in Ahp1 by Asn. The hydrophobic F83 is highly conserved or replaced by Tyr or His. Residue V84 is highly conserved except in two mitochondrial Prxs and Ahp1, where

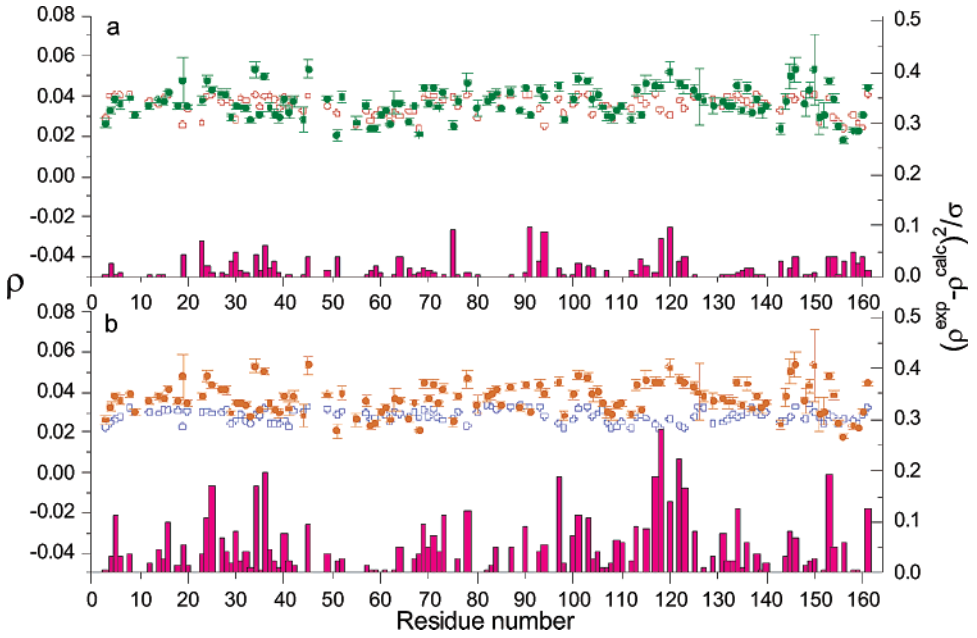

FIGURE 5: Comparison between experimental ρ factor (●) and calculated ρ factor (○) by using HydroNMR for a Prx interface perpendicular (a) and parallel (b) to the central β sheet. Open bars represent residuals $(\rho^{exp} - \rho^{calc})^2/\sigma$ between the theoretical and experimental ρ factors.

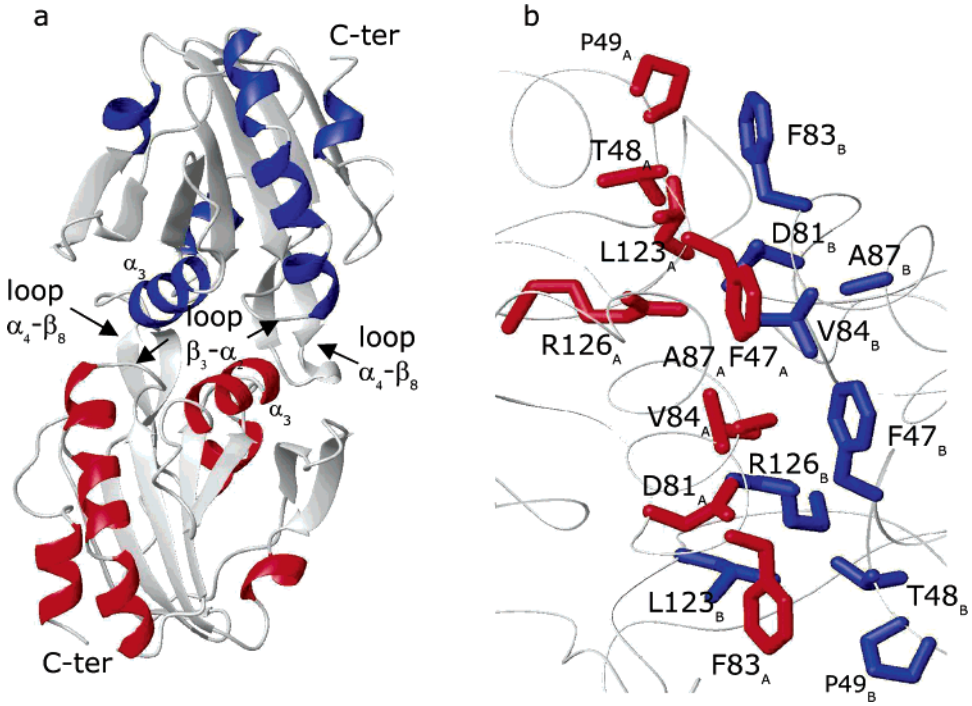

FIGURE 6: Interface of the poplar D-Prx dimer. (a) Overall view of the homodimeric Prx showing the Prx−Prx interface roughly perpendicular to the central β sheet. The regions involved in the interaction surface are indicated (see also Figure 7). (b) Zoom of the interface showing the side chains of the residues that interact to stabilize the dimer. One monomer is colored in blue, and the other monomer is colored in red.

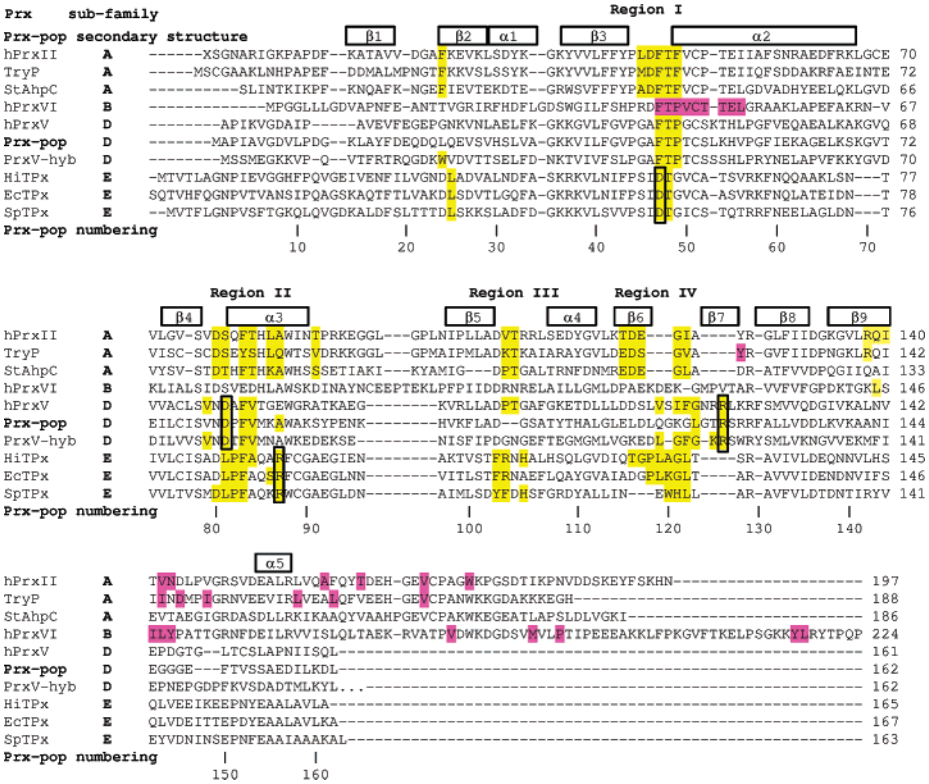

FIGURE 7: Structure-based sequence alignment of A, B, D, and E Prxs. The secondary structure elements and the numbering of the poplar Prx are indicated. The residues involved in the Prx−Prx interface of A- and B-Prx dimers (first type of interface, see the text) are colored in magenta. The residues involved in the Prx−Prx interface of D- and E-Prx dimers and in A-Prx decamers (second type of interface) are colored in yellow. Residues of D and E Prxs in boxes are involved in intermolecular salt bridges.

it is replaced by Ala. A87 is less conserved but is generally Ala, Gly, or Glu. L123 is conserved in 38% of the D Prxs or replaced by hydrophobic Phe in 40% of the sequences. Finally, R126 is strictly conserved but in Ahp1 (W). Therefore, because the interface residues are largely conserved in D (type II) Prxs, it is likely that all those proteins

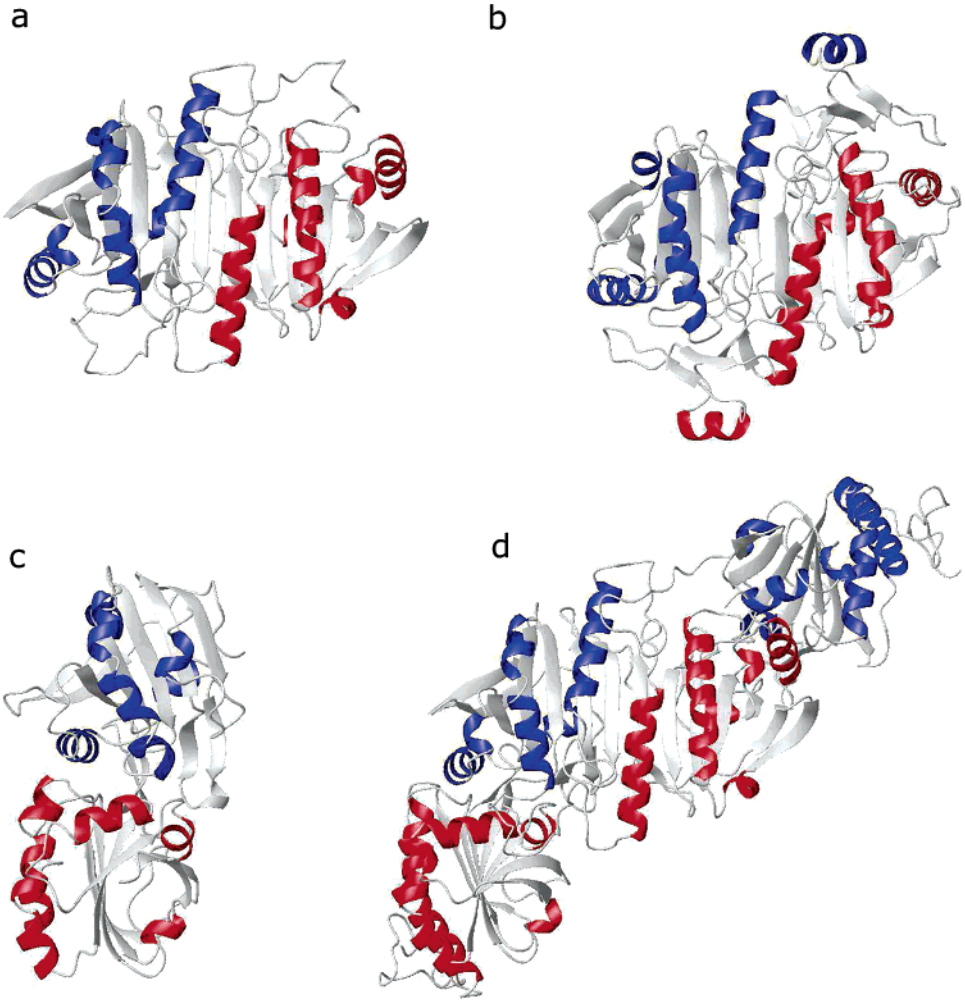

FIGURE 8: First type (a and b) and second type (c and d) of Prx−Prx interfaces in Prxs. (a) Prx−Prx interface in A-Prx dimers, first type of interface parallel to the β sheet. The Prx is the *Salmonella typhimurium* AhpC Prx (PDB entry 1N8J). (b) Prx−Prx interface in B-Prx dimers, first type of interface parallel to the β sheet (human hPrxVI, PDB entry 1PRX). (c) Prx−Prx interface in D- or E-Prx dimers, second type of interface perpendicular to the β sheet (poplar Prx, PDB entry 1TP69). (d) Prx−Prx interface in A-Prx decamers between two dimers, second type of interface perpendicular to the β sheet (*S. typhimurium* AhpC Prx, PDB entry 1N8J).

share the same Prx−Prx association perpendicular to the central β sheet.

Prx−Prx Interface of E Prxs. Recently, the structure of the *E. coli* TPx has been reported in the oxidized state, with an intramolecular disulfide bridge (*23*). The E Prx is a noncovalent dimer stabilized by hydrophobic interactions and hydrogen bonding, with Prx−Prx contacts perpendicular to the β sheet (*23*). Two other dimeric E Prx structures are available in the PDB under accession entries 1Q98 (*H. influenzae* oxidized TPx) and 1PSQ (*Streptococcus pneumoniae* reduced TPx). The residues involved in the interaction surface are located in regions similar to D Prxs (Figure 7). Moreover, the residues are more or less conserved in all known bacterial Tpxs (*23*), suggesting that most E Prxs are dimers with a Prx−Prx interface similar to D Prxs.

Prx−Prx Interfaces of A and B Prxs. The interaction surface of A- and B-Prx dimers is parallel to the β sheet, with contacts between the external strands, which form a large β sheet via a new antiparallel pairing (parts a and b of Figure 8) (*7*, *17*−*20*). The contacts are mainly hydrophobic with hydrogen bonds involving the backbone and side chains (*17*).

There is also another type of Prx−Prx interface found in the toric decamers of A Prxs (Figure 8d). This interface is found between two dimers and is stabilized by hydrophobic contacts. The interactions are located in four regions of the protein, β3−α2 (region I), β4−α3 (region II), β5−α4 (region III), and α4−β8 (region IV) (Figure 7) (*7*, *17*−*20*). The regions I and III of one monomer interacts with regions II and IV of the second monomer. The hydrophobic character of the residues is conserved within A Prxs (Figure 7). The interaction surface is similar to the interface of D- and E-Prx dimers (Figures 7 and 8).

Two Types of Prx−Prx Interfaces. Figure 8 illustrates the two types of Prx−Prx interfaces found in the Prx family. The first interface is found in the dimers of A and B Prxs and is parallel to the central β sheet (parts a and b of Figure 8). The second type of Prx−Prx interface is found in D- and E-Prx dimers and uses a surface perpendicular to the β sheet (Figures 6 and 8c). This second type of interface is also used for the oligomerization of A-Prx dimers into toric decamers (Figure 8d). This interaction surface is not accessible in B Prxs because it is the site of the C-terminal domain interaction with the core structure (Figure 8b). The residues that stabilize the interface are located in A- and B-Prx dimers in strand β9 and the C-terminal helix (A Prxs) or in the C-terminal domain (B Prxs) (Figure 7). These C-terminal regions are absent in D and E Prxs (Figure 7). Such a

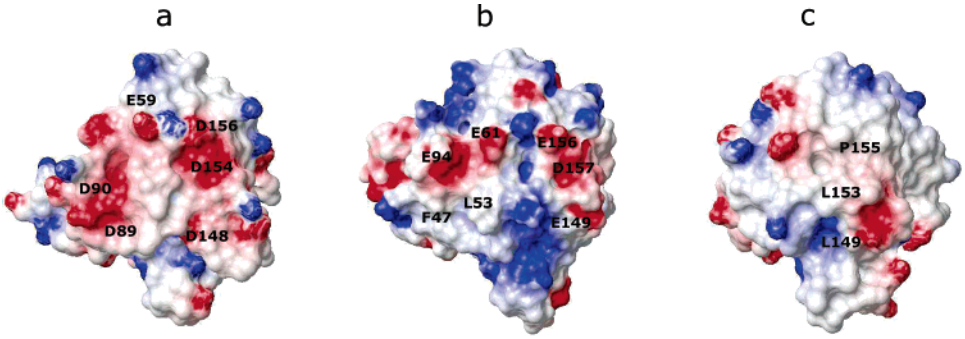

FIGURE 9: Interaction surfaces of the D Prxs with their electron donor. The figure was generated with Molmol (*48*). (a) Electrostatic potential surface of the Prx domain of the hybrid PrxV from *H. influenzae* (PDB entry 1NM3). The residues involved in the interaction with Grx are indicated. (b) Electrostatic potential surface of the poplar Prx (PDB entry 1TP69). The negatively charged residues conserved in the equivalent surface of the Prx as compared to the hybrid PrxV are labeled. The hydrophobic residue L53 that could be involved in the interaction with Trx is indicated. (c) Electrostatic potential surface of the human PrxV (PDB entry 1HD2). The hydrophobic residues that could interact with Trx are indicated.

difference in the protein sequence could explain why this type of interface parallel to the central β sheet is not observed in D and E Prxs.

In A-Prx decamers, the first type of Prx−Prx interface (parallel to the β sheet) is stronger and larger than the second interface (*17*). The dimer interaction surface reaches 1280 Å^2 per monomer for rPrxI (*18*) (A Prx, 15% of the total monomer surface), 1050 Å^2 for AhpC (*20*) (A Prx), 1700 Å^2 in hPrxVI (*7*) (B Prx, 17.4%), and 2109 Å^2 in hPrxII (*19*) (A Prx, 21%). The second type of interface (perpendicular to the β sheet) reaches 630 Å^2 in hPrxII (*19*) (7%) and 650 Å^2 in AhpC (*20*). In the structure of D Prxs, the dimer interface buries 826 Å^2 per monomer in the hybrid PrxV (*30*) (10.5%) and 785 Å^2 in the human PrxV (10.6%).

The second type of interface has been shown to be disturbed upon the formation of the disulfide bridge in A Prxs (*17*−*20*). The helix turn containing the peroxidatic cysteine unwinds, which shifts the preceding residues (region I), disrupts the interactions triggered by the residues F42 and F44 (numbering in AhpC), and dissociates the decamer into dimers (*20*). In the structure of the oxidized *E. coli* TPx (atypical 2-Cys E Prx), the dimer is not disrupted (*23*). The authors argue that Phe residues conserved in A Prxs are replaced in E Prxs by Asp and Gly (Figure 7). In D Prxs, residue F42 is conserved and F44 is replaced by a proline (Figure 7). However, the oligomerization of the hybrid PrxV (D Prx) was shown to be independent of the protein redox state by analytical ultracentrifugation, light scattering, and gel-filtration experiments (*30*), meaning that the interface is not broken upon oxidation. There must be therefore some differences between the D- and E-Prx interface as compared to the A-Prx decamer interface, which could explain the stronger stability of the interface in D and E Prxs. The most obvious difference is the presence in the latter of intermolecular salt bridges between conserved charged residues (in the squares in Figure 7). Such interactions are not present in A Prxs (Figure 7). However, the possibility that the dimer could dissociate in particular circumstances cannot be excluded. Upon dilution from 0.8 to 0.08 mM at 38 °C, the poplar Prx ^{15}N heteronuclear single-quantum coherence spectrum exhibits no significant chemical-shift differences. This indicates that the protein does not dissociate in the experimental conditions used. This fact also strongly correlates with the stable homodimer demonstrated for yeast Ahp1 using ultracentrifugation and NMR relaxation analysis (*24*).

Functional Role of the Dimerization. As shown in Figure 8, B, D, and E Prxs form dimers, whereas A Prxs switch between dimers and decamers. Very recently, the shift from low MW species to high MW complexes of A Prxs has been shown to be linked to a functional peroxidase−chaperone switch (*57*). In hPrxVI (B Prx), the dimerization has been proposed to play a role in shaping the active-site pocket. The interactions between residues of one monomer and residues of the second monomer C-terminal domain in the vicinity of the active site make the entrance narrower (*7*). The interaction surface of B-Prx C-terminal domain with the protein core is more or less equivalent to the second type of interface found in D and E Prxs (see above and parts b and d of Figure 8). Therefore, the perpendicular interface found in D- and E-Prx dimers and in reduced A-Prx decamers could play a similar role in the substrate specificity. In agreement with this, the EcTPx (E Prx) substrate-binding site has been shown to extend to the dimer interface by docking calculations (*23*). However, it would be necessary to gain experimental data to better define the substrate-binding site of Prxs.

Prx−Grx Interaction. Hybrid Prxs-containing Grx domains have been characterized in some pathogenic bacteria and in an anaerobic sulfur-oxidizing phototroph (*34*, *36*, *58*). So far, all of the Prxs that can be reduced by the Grx system are D-Prxs (*31*, *33*, *36*). The crystal structure of the hybrid PrxV from *H. influenzae* is the first direct structural information reported for the interaction of a Prx with its electron donor (*30*). The Prx and Grx domains of different monomers interact with each other through charge interactions. As already reported (*30*), two of the negatively charged residues important for the interaction are conserved in the poplar Prx (E149 and E156) and other charged residues are found in the surface (Figure 9). The equivalent surface of human PrxV is much more hydrophobic, in agreement with its specific Trx interaction only. Such an interaction is also possible for the poplar Prx (*31*) and could be explained by the presence of hydrophobic residues such as L53 and F47 (Figure 9).

Interestingly, a turn with the sequence G146-G147-G148 is located before the region that contain the residues E149, E156, and D157, important for the Grx−Prx interaction. The tripeptide could enable some protein conformational adjust-

ment upon interaction with the Grx. A glycine residue is present in this region in 82% of the D Prxs. The region D145−D157 has been shown to be predisposed to conformational change in the structure of an oxidized form of human PrxV that could correspond to a metastable state (*22*). Moreover, several residues from the 143−162 region indicate exchange terms, particularly in the 155−160 region. To better understand the Prx−Grx interaction at the structural and dynamic level, NMR experiments will be conducted to study the nature of the transient complex between Prx and Grx.

ACKNOWLEDGMENT

We thank Yves Meyer from Laboratoire Genome et Developpement des Plantes, Université de Perpignan, UMR CNRS 5096, France, for the production of *Arabidopsis thaliana* Prxs.

REFERENCES

1. Kim, K., Kim, I. H., Lee, K.-Y., Rhee, S. G., and Stadtman, E. R. (1988) The isolation and purification of a specific "protector" protein which exhibits enzyme inactivation by a thiol/Fe^{III}/O_2 mixed-function oxidation system, *J. Biol. Chem. 263*, 4704−4711.
2. Wood, Z. A., Schröder, E., Harris, J. R., and Poole, L. B. (2003) Structure, mechanism, and regulation of peroxiredoxins, *Trends Biochem. Sci. 28*, 32−40.
3. Hofmann, B., Hecht, H.-J., and Flohé, L. (2002) Peroxiredoxins, *Biol. Chem. 383*, 347−364.
4. Dietz, K.-J. (2003) Plant peroxiredoxins, *Annu. Rev. Plant Biol. 54*, 93−107.
5. Rouhier, N., and Jacquot, J.-P. (2002) Plant peroxiredoxins: Alternative hydroperoxide scavenging enzymes, *Photosynth. Res. 74*, 259−268.
6. Ellis, H. R., and Poole, L. B. (1997) Novel application of 7-chloro-4-nitrobenzo-2-oxa-1,3-diazole to identify cysteine sulphenic acid in the AhpC component of alkyl hydroperoxide reductase, *Biochemistry 36*, 15013−15018.
7. Choi, H.-J., Kang, S. W., Yang, C.-H., Rhee, S. G., and Ryu, S.-E. (1998) Crystal structure of a novel human peroxidase enzyme at 2.0 Å resolution, *Nat. Struct. Biol. 5*, 400−406.
8. Fisher, A. B., Dodia, C., Manevich, Y., Chen, J. W., and Feinstein, S. I. (1999) Phospholipid hydroperoxides are substrates for non-selenium glutathione peroxidase, *J. Biol. Chem. 274*, 21326−21334.
9. Peshenko, I. V., and Shishi, H. (2001) Oxidation of active center cysteine of bovine 1-cys peroxiredoxin to the cysteine sulphenic acid form by peroxide and peroxynitrite, *Free Radical Biol. Med. 31*, 292−303.
10. Lee, S. P., Hwang, Y. S., Kim, Y. J., Kwon, K.-S., Kim, H. J., Kim, K., and Chae, H. Z. (2001) Cyclophilin A binds to peroxiredoxins and activates its peroxidase activity, *J. Biol. Chem. 276*, 29826−29832.
11. Chae, H. Z., Chung, S. J., and Rhee, S. G. (1994) Thioredoxin-dependent peroxide reductase from yeast, *J. Biol. Chem. 269*, 27670−27678.
12. Nogoceke, E., Gommel, D. U., Kiess, M., Kalisz, H. M., and Flohé, L. (1997) A unique cascade of oxidoreductases catalyses trypanothione-mediated peroxide metabolism in *Crithidia fasciculata*, *Biol. Chem. 378*, 827−836.
13. Bryk, R., Lima, C. D., Erdjument-Bromage, H., Tempst, P., and Nathan, C. (2002) Metabolic enzymes of mycobacteria linked to antioxidant defense by a thioredoxin-like protein, *Science 295*, 1073−1077.
14. Poole, L. B., Reynolds, C. M., Wood, Z. A., Karplus, P. A., Ellis, H. R., and Calzi, M. L. (2000) AhpF and other NADH: peroxiredoxin oxidoreductases, homologues of low Mr thioredoxin reductase, *Eur. J. Biochem. 267*, 6126−6133.
15. Sayed, A. A., and Williams, D. L. (2004) Biochemical characterization of 2-Cys peroxiredoxins from *Schistosoma mansoni*, *J. Biol. Chem. 279*, 26159−26166.
16. Seo, M. S., Kang, S. W., Kim, K., Baines, I. C., Lee, T. H., and Rhee, S. G. (2000) Identification of a new type of mammalian peroxiredoxin that forms an intramolecular disulphide as a reaction intermediate, *J. Biol. Chem. 275*, 20346−20354.
17. Alphey, M. S., Bond, C. S., Tétaud, E., Fairlamb, A. H., and Hunter, W. N. (2000) The structure of reduced tryparedoxin peroxidase reveals a decamer and insight into reactivity of 2Cys-peroxiredoxins, *J. Mol. Biol. 300*, 903−916.
18. Hirotsu, S., Abe, Y., Okada, K., Nagahara, N., Hori, H., Nishino, T., and Hakoshima, T. (1999) Crystal structure of a multifunctional 2-Cys peroxiredoxin heme-binding protein 23 kDa/proliferation-associated gene product, *Proc. Natl. Acad. Sci. U.S.A. 96*, 12333−12338.
19. Schröder, E., Littlechild, J. A., Lebedev, A. A., Erringhton, N., Vagin, A. A., and Isupov, M. N. (2000) Crystal structure of decameric 2-Cys peroxiredoxin from human erythrocytes at 1.7 Å resolution, *Structure 8*, 605−615.
20. Wood, Z. A., Poole, L. B., Hantgan, R. R., and Karplus, P. A. (2002) Dimers to doughnuts: Redox-sensitive oligomerization of 2-cysteine peroxiredoxins, *Biochemistry 41*, 5493−5504.
21. Declercq, J.-P., Evrard, C., Clippe, A., van der Stricht, D., Bernard, A., and Knoops, B. (2001) Crystal structure of human peroxiredoxin 5, a novel type of mammalian peroxiredoxin at 1.5 Å resolution, *J. Mol. Biol. 311*, 751−759.
22. Evrard, C., Capron, A., Marchand, C., Clippe, A., Wattiez, R., Soumillion, P., Knoops, B., and Declercq, J.-P. (2004) Crystal structure of a dimeric oxidized form of human peroxiredoxin 5, *J. Mol. Biol. 337*, 1079−1090.
23. Choi, J., Choi, S., Choi, J., Cha, M.-K., Kim, I.-H., and Shin, W. (2003) Crystal struture of *Escherichia coli* thiol peroxidase in the oxidized state: Insights into intramolecular disulphide formation and substrate binding in atypical 2-Cys peroxiredoxins, *J. Biol. Chem. 278*, 49478−49486.
24. Trivelli, X., Krimm, I., Ebel, C., Verdoucq, L., Prouzet-Mauléon, V., Chartier, Y., Tsan, P., Lauquin, G., Meyer, Y., and Lancelin, J.-M. (2003) Characterization of the yeast peroxiredoxin Ahp1 in its reduced active and overoxidized inactive forms using NMR, *Biochemistry 42*, 14139−14149.
25. Kong, W., Shiota, S., Shi, Y., Nakayama, H., and Nakayama, K. (2000) A novel peroxiredoxin of the plant *Sedum lineare* is a homologue of *Escherichia coli* bacterioferritin co-migratory protein (Bcp), *Biochem. J. 351*, 107−114.
26. Rouhier, N., Gelhaye, E., Gualberto, J. M., Jordy, M. N., De Fay, E., Hirasawa, M., Duplessis, S., Lemaire, S. D., Frey, P., Martin, F., Manieri, W., Knaff, D. B., and Jacquot, J.-P. (2004) Poplar peroxiredoxin Q. A thioredoxin-linked chloroplast antioxidant functional in pathogen defense, *Plant Physiol. 134*, 1027−1038.
27. Jeong, J. S., Kwon, S. J., Kang, S. W., Rhee, S. G., and Kim, K. (1999) Purification and characterization of a second type thioredoxin peroxidase (type II TPx) from *Saccharomyces cerevisiae*, *Biochemistry 38*, 776−783.
28. Verdoucq, L., Vignols, F., Jacquot, J.-P., Chartier, Y., and Meyer, Y. (1999) *In vivo* characterization of a thioredoxin h target protein defines a new peroxiredoxin family, *J. Biol. Chem. 274*, 19714−19722.
29. Lee, J., Spector, D., Godon, C., Labarre, J., and Toledano, M. B. (1999) A new antioxidant with alkyl hydroperoxide defense properties in yeast, *J. Biol. Chem. 274*, 4537−4544.
30. Kim, S. J., Woo, J. R., Hwang, Y. S., Jeong, D. G., Shin, D. H., Kim, K., and Ryu, S. E. (2003) The tetrameric structure of *Haemophilus influenzae* hybrid-Prx5 reveals interactions between electron donor and acceptor proteins, *J. Biol. Chem. 278*, 10790−10798.
31. Rouhier, N., Gelhaye, E., Sautière, P.-E., Brun, A., Laurent, P., Tagu, D., Gérard, J., de Fay, E., Meyer, Y., and Jacquot, J.-P. (2001) Isolation and characterization of a new peroxiredoxin from poplar sieve tubes that uses either glutaredoxin or thioredoxin as a proton donor, *Plant Physiol. 127*, 1299−1309.
32. Rouhier, N., Gelhaye, E., and Jacquot, J.-P. (2002) Glutaredoxin dependent peroxiredoxin from poplar: Protein−protein interaction and catalytic mechanism, *J. Biol. Chem. 277*, 13609−13614.
33. Bréhelin, C., Meyer, E. H., De Souris, J.-P., Bonnard, G., and Meyer, Y. (2003) Resemblance and dissemblance of *Arabidopsis* type II peroxiredoxins: Similar sequences for divergent gene expression, protein localization, and activity, *Plant Physiol. 132*, 2045−2057.
34. Hwang, Y. S., Chae, H. Z., and Kim, K. (2000) Characterization of *Haemophilus influenzae* Peroxiredoxins, *J. Biochem. Mol. Biol. 33*, 514−518.
35. Pauwels, F., Vergauwen, B., Vanrobaeys, F., Devreese, B., and van Beeumen, J. J. (2003) Purification and characterization of a chimeric enzyme from *Haemophilus influenzae* Rd that exhibits

glutathione-dependent peroxidase activity, *J. Biol. Chem. 278*, 16658−16666.
36. Rouhier, N., and Jacquot, J.-P. (2003) Molecular and catalytic properties of a peroxiredoxin-glutaredoxin hybrid from *Neisseria meningitidis*, *FEBS Lett. 554*, 149−153.
37. Echalier, A., Corbier, C., Rouhier, N., Jacquot, J.-P., and Aubry, A. (2002) Crystallization and preliminary X-ray data of a bifunctional peroxiredoxin from poplar, *Acta Crystallogr., Sect. D 58*, 1501−1503.
38. Bouillac, S., Rouhier, N., Tsan, P., Jacquot, J.-P., and Lancelin, J.-M. (2004) ^{1}H, ^{13}C, and ^{15}N NMR assignment of the homodimeric poplar phloem type II peroxiredoxin, *J. Biomol. NMR 30*, 105−106.
39. Brünger, A. T., Adams, P. D., Clore, G. M., DeLano, W. L., Gros, P., Grosse-Kunsteleve, R. W., Jiang, J. S., Kuszewski, J., Nilges, M., Pannu, N. S., Read, R. J., Rice, L. M., Simonson, T., and Warren, G. L. (1998) Crystallography and NMR system: A new software suite for macromolecular structure determination, *Acta Crystallogr., Sect. D 54*, 905−921.
40. Roussel, P. A., and Cambillau, C. (1991) *TURBO−FRODO, Silicon Graphics Applications Directory*, Silicon Graphics, Mountain View, CA.
41. Murshudov, G. N., Vagin, A. A., Lebedev, A., Wilson, K. S., and Dodson, E. J. (1999) Efficient anisotropic refinement of macromolecular structures using FFT, *Acta Crystallogr., Sect. D 55*, 247−255.
42. Laskowsky, R. A., MacArthur, M. W., Moss, D. S., and Thornton, J. M. (1993) PROCHECK: A program to check the stereochemical quality of protein structures, *J. Appl. Crystallogr. 26*, 283−291.
43. Farrow, N. A., Muhandiram, R., Singer, A. U., Pascal, S. M., Kay, C. M., Gish, G., Shoelson, S. E., Pawson, T., Forman-Kay, J. D., and Kay, L. E. (1994) Backbone dynamics of a free and phosphopeptide-complexed Src homology 2 domain studied by ^{15}N NMR relaxation, *Biochemistry 33*, 5984−6003.
44. Fushman, D., Xu, R., and Cowburn, D. (1999) Direct determination of changes of interdomain orientation on ligation: Use of the orientational dependence of ^{15}N NMR relaxation in Abl SH(32), *Biochemistry 38*, 10225−10230.
45. Fushman, D., Cowburn, D., and Tjandra, N. (1999) An approach to direct determination of protein dynamics from ^{15}N NMR relaxation at multiple fields, independent of variable ^{15}N chemical shift anisotropy and chemical exchange contributions, *J. Am. Chem. Soc. 121*, 8577−8582.
46. Fushman, D., and Cowburn, D. (2001) Nuclear magnetic resonance relaxation in determination of residue-specific ^{15}N chemical shift tensors in proteins in solution: Protein dynamics, structure, and applications of transverse relaxation optimized spectroscopy, *Methods Enzymol. 339*, 109−126.
47. Fushman, D., and Cowburn, D. (2002) Characterization of interdomain orientations in solutions using the NMR relaxation approach, in *Protein NMR for the Millenium* (Krishna, N. R., Ed.) pp 53−78, Kluwer, Norwell, MA.
48. Koradi, R., Billeter, M., and Wuthrich, K. (1996) MOLMOL: A program for display and analysis of macromolecular structures, *J. Mol. Graphics 14*, 51−55.
49. Walker, O., Varadan, R., and Fushman, D. (2004) Efficient and accurate determination of the overall rotational diffusion tensor of a molecule from ^{15}N relaxation data using computer program ROTDIF, *J. Magn. Reson. 168*, 336−345.
50. Garcia de la Torre, J., Huertas, M. L., and Carrasco, B. (2000) HYDRONMR: Prediction of NMR relaxation of globular proteins from atomic-level structures and hydrodynamic calculations, *J. Magn. Reson. 147*, 138−146.
51. Bernado, P., Garcia de la Torre, J., and Pons, M. (2002) Interpretation of ^{15}N NMR relaxation data of globular proteins using hydrodynamic calculations with HYDRONMR, *J. Biomol. NMR 23*, 139−150.
52. Sali, A., Potterton, L., Yuan, F., van Vlijmen, H., and Karplus, M. (1995) Evaluation of comparative protein modeling by MODELLER, *Proteins 23*, 318−326.
53. Cornilescu, G., Delaglio, F., and Bax, A. (1999) Protein backbone angle restraints from searching a database for chemical shift and sequence homology, *J. Biomol. NMR 13*, 289−302.
54. Rouhier, N., Gelhaye, E., Corbier, C., and Jacquot, J.-P. (2004) Active site mutagenesis and phospholipid hydroperoxide reductase activity of poplar type II peroxiredoxin, *Physiol. Plant. 120*, 57−62.
55. Åkerud, T., Thulin, E., van Etten, R. L., and Akke, M. (2002) Intramolecular dynamics of low molecular weight protein tyrosine phosphatase in monomer−dimer equilibrium studied by NMR: A model for changes in dynamics upon target binding, *J. Mol. Biol. 322*, 137−152.
56. Fushman, D., Ghose, R., and Cowburn, D. (2000) The effect of finite sampling on the determination of orientational properties: A theoretical treatment with application to interatomic vectors in proteins, *J. Am. Chem. Soc. 122*, 10640−10649.
57. Jang, H. H., Lee, K. O., Chi, Y. H., Jung, B. G., Park, S. K., Park, J. H., Lee, J. R., Lee, S. S., Moon, J. C., Yun, J. W., Choi, Y. O., Kim, W. Y., Kang, J. S., Cheong, G. W., Yun, D. J., Rhee, S. G., Cho, M. J., and Lee, S. Y. (2004) Two enzymes in one; two yeast peroxiredoxins display oxidative stress-dependent switching from a peroxidase to a molecular chaperone function, *Cell 117*, 625−635.
58. Vergauwen, B., Pauwels, F., Jacquemotte, F., Meyer, T., Cusanovich, M., Bartsch, R., and Beeumen, J. (2001) Characterization of glutathione amide reductase from *Chromatium gracile*, *J. Biol. Chem. 276*, 20890−20897.
59. Kabsch, W. (1976) A solution for the best rotation to relate two sets of vectors, *Acta Crystallogr., Sect. A 32*, 922−923.

BI048226S